Title

Fatigue crack growth in polysilicon microstructures subjected to multi-axial loading: A Poisson–Voronoi-based finite element analysis

Authors

Xu, Rui
Komvopoulos, Kyriakos

Publication Date

2023-12-01

DOI

10.1016/j.ijfatigue.2023.107898

Peer reviewed

International Journal of Fatigue 177 (2023) 107898

Contents lists available at ScienceDirect

International Journal of Fatigue

journal homepage: www.elsevier.com/locate/ijfatigue

Fatigue crack growth in polysilicon microstructures subjected to multi-axial loading: A Poisson–Voronoi-based finite element analysis

Rui Xu [a], Kyriakos Komvopoulos [a,*]

[a] Department of Mechanical Engineering, University of California, Berkeley, CA 94720, USA

ARTICLE INFO

Keywords:
Cracks
Crystalline materials
Fatigue
Finite element analysis
Fracture

ABSTRACT

Polycrystalline silicon (polysilicon) is the most commonly used structural material of microscopic electromechanical devices, such as sensors and actuators. Almost all of these miniaturized devices contain mechanical elements experiencing high-frequency loading cycles. Due to the rapidly accumulating loading cycles and very small thicknesses of these microstructures, basic understanding of fatigue crack growth in polysilicon at the microscale is critical to the design of durable microdevices that satisfy application requirements. In this investigation, fatigue crack growth in a typical polysilicon microstructure subjected to multi-axial loading was analyzed with the finite element method. To account for the inherent heterogeneity and anisotropy of polysilicon at the microscale, a Poisson-Voronoi tessellation was incorporated in the highly stressed region of the resonating microdevice to model a polycrystalline microstructure. Simulation results illuminated the effect of local texture on the direction and rate of crack growth. Transgranular or intergranular crack growth were predicted, depending on the angle between the crack-path direction and the grain boundary and the fracture resistance of the grain and the grain boundary. From a fundamental fracture mechanics perspective, the computational approach developed in this study provides a capability for examining the effect of local texture anisotropy on cracking in polycrystalline microstructures.

1. Introduction

Dynamic electromechanical microdevices have been undergoing swift developments and increased industrial utilization. A variety of such microdevices have entered the microelectronics and communications marketplace, including high-resolution displays, high-density data storage, inkjet print heads, and pressure sensors and accelerometers used in the automobile industry. Despite variations in design and functionality, these microdevices share two important characteristics – they are principally made of polycrystalline silicon (polysilicon) and are generally subjected to millions or even billions of mixed-mode loading cycles during their lifetime. With device miniaturization advancing at a fast pace, long-term structural stability and endurance have become critically important for most applications. For these reasons, knowledge of microscale cracking in polysilicon, i.e., the main structural material of electromechanical components, is of paramount importance to the design of durable dynamic microdevices.

Numerous studies performed with various surface micromachined microstructures have been carried out to elucidate crack growth in silicon. For instance, fracture tests with silicon microcantilevers revealed crack initiation and growth at the lower surface energy (1 1 1) planes and cracking along the (1 1 0) planes of silicon [1,2]. Stable crack growth with increasing crack length in pre-cracked single-crystal silicon microcantilevers tested at resonance was associated with a rate-limiting mechanism triggered by the reaction of species accumulating at the crack tip [3]. Premature failure of single-crystal silicon films subjected to a fully reversed stress equal to about one-half of the fracture strength in an atmosphere that contained water vapor was accredited to environmentally-assisted cracking of the surface oxide film [4,5]. Stress-corrosion cracking of the surface oxide film of notched polysilicon microcantilevers tested at resonance in the presence of high humidity levels was claimed to be a precursor of fatigue failure [5,6]. Subcritical crack growth in polysilicon was related to the synergistic effects of water and stress [7].

Despite important insight into polysilicon fatigue obtained from previous investigations (and several others), the simple microdevices used in these experiments did not simulate fatigue under multi-axial loading conditions that are typical of those encountered with most

* Corresponding author.
E-mail address: kyriakos@me.berkeley.edu (K. Komvopoulos).

https://doi.org/10.1016/j.ijfatigue.2023.107898
Received 1 June 2023; Received in revised form 14 August 2023; Accepted 16 August 2023
Available online 30 August 2023

micromachines. In addition, the probe tips or load cells used to actuate the surface micromachined specimens were prone to significant errors in force measurement and erroneous determination of the microscopic displacements of moving structural elements. Furthermore, because the majority of micromachines are hermetically packaged, their working environment is devoid of significant traces of oxygen or water vapor, which are required for environmentally-induced cracking to play a dominant role in fatigue behavior. To circumvent the foregoing inadequacies, on-chip electrostatic actuation of special fatigue resonators allowing for effective load and displacement control compared to the methods used in the aforementioned studies was developed for studying multi-axial fatigue of polysilicon microstructures in controlled atmospheres [8,9].

Furthermore, with the accelerating reduction in size of polysilicon microstructures, the inherent heterogeneity and anisotropy of polycrystalline microstructures assumed an even greater importance in fatigue crack growth. Due to the alternating orientation, size, and shape of polysilicon crystals (grains), the mechanical behavior at the microscale can be strongly anisotropic. For example, the elastic anisotropy of crystals and the stress singularities arising at grain corners [10–12] can greatly affect the stress distribution at the grain level, further exacerbating stress singularity effects, depending on the anisotropy and orientation of the grains [12]. Grain orientation-induced local anisotropy may lead to large variations of the stress intensity factor (SIF) when the crack size is of the order of a few grain diameters [13]. Grain anisotropy in a nickel-based superalloy yielded a stepwise variation of the J-integral with the crack length, which was attributed to changes in transgranular crack growth rate [14]. Consequently, stochastic methods were used to account for the effect of local anisotropy at the microscale. For example, Monte Carlo-finite element method (FEM) modeling was used to predict the nominal elastic constants of a thin-film aggregate of cubic crystals and compare them with plane-strain Voigt and Reuss bounds [15]. In another Monte Carlo-FEM study [16], consistent statistical results of the microscopic (local) SIFs and the energy release rate of a crack embedded in a columnar aggregate of randomly oriented, perfectly bonded, orthotropic crystals were computed for a given level of anisotropy, on condition that the crack tip was surrounded by at least ten grains. The implementation of the Poisson-Voronoi Diagram (PVD), which is topologically equivalent to the microstructure of real ceramics and metals, in stress analyses of polycrystalline aggregates revealed systematic variations in micro-stress [17]. A PVD was incorporated in FEM models of polysilicon micromachines to examine the effects of local inhomogeneity and anisotropy of polysilicon on the stress distribution in the critical region of planar surface micromachines at resonance [18].

A variety of FEM models have been developed for studying crack growth in materials, including the element-free Galerkin (EFG) method [19], the extended FEM (XFEM) [20,21], and the cohesive surface formulation (CSF) method [22–24]. The EFG method uses a fracture process zone that allows for arbitrary direction and rate of crack growth. The XFEM is an embedded discontinuity approach that relies on a partition-of-unity-based enrichment method for discontinuous fields; however, even though remeshing due to crack advancement is not required, special functions must be used to span the asymptotic near-tip displacement field. The CSF method is based on a phenomenological framework in which the fracture characteristics of the material are embedded in a cohesive surface traction-displacement relation, obeyed by interface elements placed along a predetermined crack path, which are used to simulate grain boundary shearing and fracture. Grain-level micromechanics modeling of material constitutive behavior under quasi-static and dynamic loading was accomplished by a stochastic analysis of the size distribution, morphology, and location of initial defects in a representative volume element composed of a set of grains [24,25]; however, only intergranular fracture was modeled due to the limitations of the adopted cohesive surface formulation method. Molecular statistics simulations of single-edge cracked silicon samples demonstrated scale dependence of the fracture process zone at a critical size of a few nanometers, suggesting that brittle fracture was governed by atomic bond breakage [26].

In the present study, a PVD-FEM approach was developed to analyze subcritical fatigue crack growth from a tiny crack embedded in the critical region of a polysilicon microstructure. There are two main advantages for selecting this approach. First, the use of a standard FEM formulation does not require special functions, and second, arbitrary crack paths can be modelled since there is no need to introduce interface elements in the model, consequently enabling the simulation of both intergranular and transgranular fracture. Numerical results of multiaxial fatigue crack growth are presented for the most prevalent micromachine polysilicon textures {1 1 0} and {1 0 0} to elucidate the effect of local anisotropy (i.e., grain orientation, size, and shape) on the tendency for transgranular and intergranular fatigue crack growth.

2. Methods

2.1. Model

Special micromachines that can generate sufficiently high stresses at resonance are desirable for investigating fatigue damage at the microscale. In addition, on-chip actuation is more advantageous than macroscale testing because the generated force can be easily controlled and force measurement errors occurring with macroscale loading techniques can be avoided. Fig. 1 shows a scanning electron microscope (SEM) micrograph of a planar resonator, specifically designed for simulating multi-axial fatigue of a two-beam suspension microstructure [8,9]. The main components of the resonator are the two long beams attached to a rotational ring at one end and anchored to the substrate at the other end, which play the role of the fatigue microstructures, a suspended ring structure acting as a connector, and six comb-structures divided in two groups A and B that provide driving and sensing capabilities, respectively. To enhance the visual measurement of the in-plane rotation angle, two of the radial spokes were extended with verniers at the tips. Matching sets of stationary indicator marks were placed near the end to allow visual measurement of angular movements as small as 0.1°. Since an electrostatic driving force cannot statically generate sufficiently high stresses in the two-beam suspension, the micromachine must be resonated to initiate the damage process.

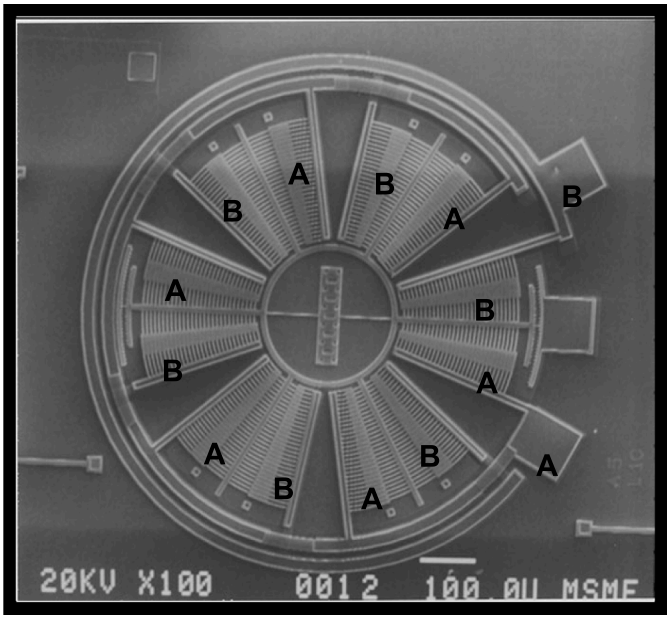

Fig. 1. SEM micrograph of a two-beam resonator. Six comb drives are divided into two groups A and B, one for electrostatic force driving and the other for capacitive sensing and control.

2.2. Finite element modeling procedure

Since polysilicon exhibits a predominant columnar microstructure [27–29], the through-thickness material properties were presumed to be approximately uniform. Therefore, two-dimensional FEM modeling was used to analyze fatigue crack growth in the critical beam-anchor region of the two-beam micromachine. To examine the effect of the orientation, shape, and size distribution of the silicon grains, the polycrystalline microstructure in the critical micromachine region was modeled with a PVD, using an approach based on a given mean grain diameter developed in another study [18]. Micromachine beams with the appropriate polycrystalline structures were modeled by importing the generated PVD into the MSC Patran code and subsequently mapping the micromachine geometry onto the PVD. For computational efficiency, only the critical region of the micromachine FEM models (i.e., the beam-anchor region of the polycrystalline microstructure) was modeled with the PVD.

Fig. 2(a) shows the FEM mesh of the examined two-beam micromachine. Due to the symmetric geometry and the boundary conditions, only one-half of the micromachine structure was modeled. To prevent stress singularities at the beam-anchor and beam-ring connections, 0.8-μm-radius fillets (measured from SEM images of the micromachine) were introduced in the FEM models. Fig. 2(c) shows a polycrystalline microstructure in the beam-anchor region of the FEM mesh, with six neighboring grains indexed. A 15-nm-long crack perpendicular to the beam edge was introduced in the mesh of grain (1) in the highly stressed region. The initial crack length was of the order of the root-mean-square roughness of doped and annealed polysilicon thin films. To account for the square root stress singularity at the crack tip, an annulus of collapsed quadrilateral fracture elements [30] was incorporated around the crack tip (Fig. 2(b)). The FEM meshes were refined until stress convergence was achieved. The meshes with a polycrystalline microstructure included in the critical micromachine region comprised about 11,000 eight-node, plane-stress, biquadratic elements with about 35,000 nodes. In all FEM meshes, the anchor nodes were fully constrained and the symmetry condition of the cross-sectional nodes of the suspended ring was satisfied by applying multi-point constraints. A static stress analysis [18] that yielded similar results with a computationally excessive dynamic stress analysis of the micromachine at the peak rotational angle of the ring achieved at resonance was used to compute the stresses at the crack tip and, consecutively, calculate the SIFs used in the crack growth analysis. Based on a dynamic analysis of the micromachine actuated at resonance [18], a displacement $u = 2$ μm was applied to the tip of the suspension beam, as shown in Fig. 2(a).

2.3. Polysilicon microstructure

Low-pressure chemical vapor deposition (LPCVD) is the most common process for depositing polysilicon structural layers. The growth of amorphous or polycrystalline silicon depends on the vacuum pressure and deposition temperature. For instance, LPCVD temperatures below ~600 °C produce amorphous silicon, whereas temperatures above 600 °C produce polycrystalline silicon [27–29]. LPCVD-synthesized polysilicon usually possesses columnar grains and a texture strongly depended on deposition temperature, pressure, and doping [27–29]. For deposition temperatures between 620 and 650 °C, the prevalent out-of-plane texture is {1 1 0}, with the {1 0 0} texture progressively becoming dominant as the deposition temperature is raised to 700 °C [28]. Even though {1 1 0} is the most dominant texture in polysilicon micromachines [31–33], both {1 1 0} and {1 0 0} textures with columnar grains through the thickness of the polysilicon structure were examined in this study. In addition to the out-of-plane texture of polysilicon, the mean grain size also exhibits a strong dependence on deposition temperature and pressure. Assuming circular cross sections for the columnar grains, the mean grain diameter of polysilicon deposited under different conditions was estimated to be in the range of 0.1–0.4 μm [28]. Consequently, a 0.38 μm mean grain diameter was chosen to represent the average grain size in the numerical simulations of this study.

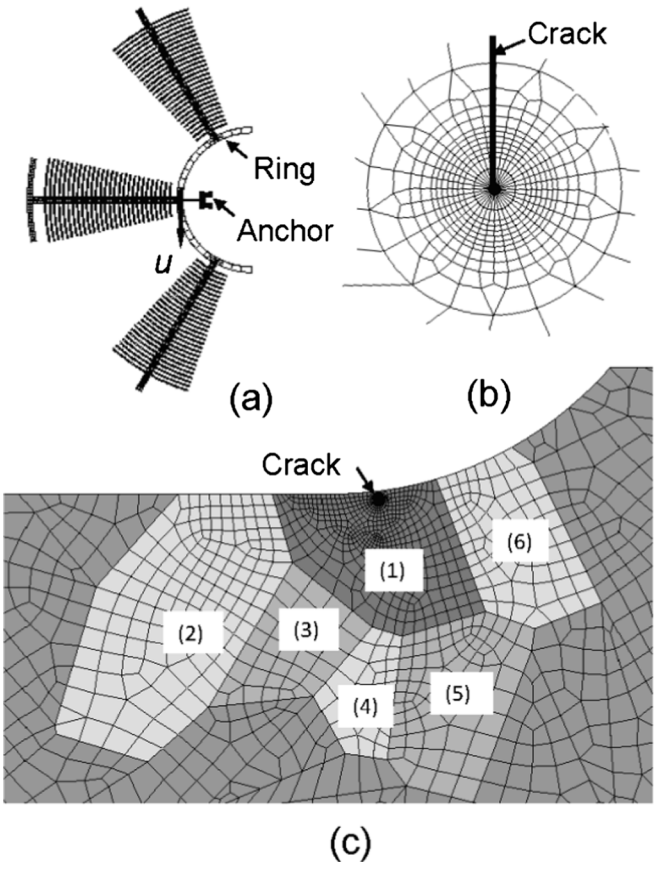

Fig. 2. (a) FEM mesh of a two-beam (30 × 2 × 2 μm) resonator, (b) detail of the mesh around the crack tip, and (c) detail of mesh in the critical beam-anchor region with six neighboring grains indexed.

2.4. Effective elastic modulus

In the crystal-axis coordinate system, the stiffness matrix **C** of single-crystal silicon is given by [34]

$$\boldsymbol{C} = \begin{bmatrix} 165.6 & 63.8 & 63.8 & 0 & 0 & 0 \\ 63.8 & 165.6 & 63.8 & 0 & 0 & 0 \\ 63.8 & 63.8 & 165.6 & 0 & 0 & 0 \\ 0 & 0 & 0 & 79.5 & 0 & 0 \\ 0 & 0 & 0 & 0 & 79.5 & 0 \\ 0 & 0 & 0 & 0 & 0 & 79.5 \end{bmatrix} \text{GPa} \quad (1)$$

The effective elastic modulus E_1^{eff} along the beam length for different textures obtained by transformation [35,36] is shown in Fig. 3. It is noted that the {1 1 0} texture demonstrates a higher range of E_1^{eff} than the {1 0 0} texture and that the periodicity of the {1 1 0} and {1 0 0} textures is 180° and 90°, respectively. An in-plane orientation angle was randomly defined for each grain in the critical region. For the beam structure outside the critical region, the effective elastic modulus was

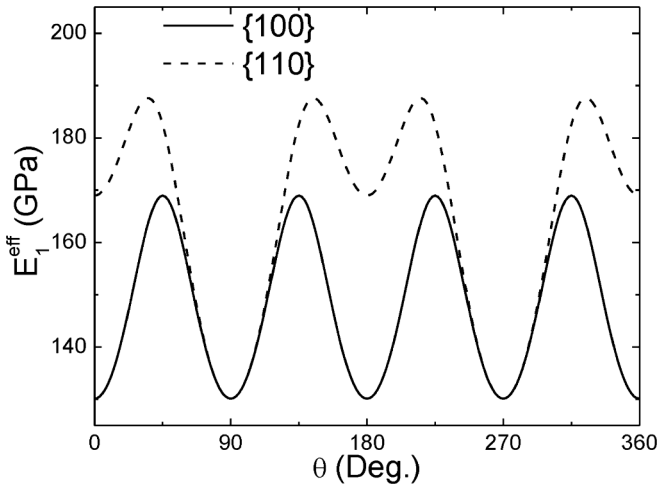

Fig. 3. Effective elastic modulus E_1^{eff} in the length direction of the beam versus in-plane orientation angle θ for {100} and {110} texture.

determined by the Voigt-Reuss-Hill (VRH) average, which is the best possible estimate when only the orientation distribution function of a polycrystalline material is known [37]. The calculated VRH average for the {110} and {100} textures was found to be equal to 166 and 149 GPa, respectively.

2.5. Crack growth

In linear elastic fracture mechanics (LEFM), the mode I and mode II SIFs, K_{I} and K_{II}, respectively, are defined by

$$\begin{aligned} K_{\text{I}} &= \lim_{r,\theta\to 0}\sqrt{2\pi r}\sigma_{yy}(r,\theta) \\ K_{\text{II}} &= \lim_{r,\theta\to 0}\sqrt{2\pi r}\tau_{xy}(r,\theta) \end{aligned} \tag{2}$$

where (r,θ) and (x,y) are cylindrical polar and Cartesian coordinates, respectively, centered at the crack tip.

For a node on the crack plane, the corresponding mode I and mode II SIFs, K_{I}^* and K_{II}^*, respectively, can be calculated by

$$\begin{aligned} K_{\text{I}}^* &= \sqrt{2\pi r^*}\sigma_{yy}(r^*,0) \\ K_{\text{II}}^* &= \sqrt{2\pi r^*}\tau_{xy}(r^*,0) \end{aligned} \tag{3}$$

where r^* is the distance of a node from the crack tip and the tensile and shear stresses $\sigma_{yy}(r^*,0)$ and $\tau_{xy}(r^*,0)$ are the stresses at that node. The actual values of K_{I} and K_{II} can be obtained by linear extrapolation to $r^*=0$ of a least-square line fit through the K_{I}^* and K_{II}^* data [38].

To determine the crack growth direction, it was necessary to calculate the tensile and shear SIFs, K_σ and K_τ, respectively, at different angles φ measured from the initial crack plane, defined by

$$\begin{aligned} K_\sigma(\varphi) &= \sqrt{2\pi r}\sigma_{\varphi\varphi}(r,\varphi) \\ K_\tau(\varphi) &= \sqrt{2\pi r}\tau_{r\varphi}(r,\varphi) \end{aligned} \tag{4}$$

with the actual values of K_σ and K_τ obtained by linear extrapolation of the least-square line fit through the K_{I}^* and K_{II}^* data, as mentioned previously.

For anisotropic materials, K_σ and K_τ are expressed by [39]

$$\begin{aligned} K_\sigma &= K_{11}K_{\text{I}} + K_{12}K_{\text{II}} \\ K_\tau &= K_{21}K_{\text{I}} + K_{22}K_{\text{II}} \end{aligned} \tag{5}$$

where K_{I} and K_{II} are the mode I and mode II SIFs, respectively, obtained from the FEM analysis, and the four coefficients in Eq. (5) are given by

$$\begin{aligned} K_{11} &= \text{Re}\left\{\frac{1}{\lambda_2-\lambda_1}\left[\lambda_2(\cos\varphi+\lambda_1\sin\varphi)^{3/2} - \lambda_1(\cos\varphi+\lambda_2\sin\varphi)^{3/2}\right]\right\} \\ K_{12} &= \text{Re}\left\{\frac{1}{\lambda_2-\lambda_1}\left[(\cos\varphi+\lambda_1\sin\varphi)^{3/2} - (\cos\varphi+\lambda_2\sin\varphi)^{3/2}\right]\right\} \\ K_{21} &= \text{Re}\left\{\frac{1}{\lambda_2-\lambda_1}\left[\lambda_2(\cos\varphi+\lambda_1\sin\varphi)^{1/2}(\sin\varphi-\lambda_1\cos\varphi)\right.\right. \\ &\quad \left.\left. - \lambda_1(\cos\varphi+\lambda_2\sin\varphi)^{1/2}(\sin\varphi-\lambda_2\cos\varphi)\right]\right\} \\ K_{22} &= \text{Re}\left\{\frac{1}{\lambda_2-\lambda_1}\left[(\cos\varphi+\lambda_1\sin\varphi)^{1/2}(\sin\varphi-\lambda_1\cos\varphi)\right.\right. \\ &\quad \left.\left. - (\cos\varphi+\lambda_2\sin\varphi)^{1/2}(\sin\varphi-\lambda_2\cos\varphi)\right]\right\} \end{aligned} \tag{6}$$

where λ_1 and λ_2 are the roots with a positive imaginary part of the characteristic equation

$$S_{11}\lambda^4 - 2S_{16}\lambda^3 + (2S_{12}+S_{66})\lambda^2 - 2S_{26}\lambda + S_{22} = 0 \tag{7}$$

where S_{ij} are components of the compliance matrix $\mathbf{S}$ of single-crystal silicon with a Cartesian coordinate system affixed to the crack tip.

There are three commonly used fracture criteria for determining the crack growth direction, namely maximum K_{I}, zero K_{II}, and maximum energy-release rate for quasi-static crack growth. Although these criteria lead to similar results for isotropic materials, crack path predictions for anisotropic materials have been reported to differ [40-42]. Instead, a fracture criterion based on the fracture resistance (surface energy) of the cleavage plane and the tensile stress normal to the cleavage plane can be used to predict crack growth in anisotropic materials [41,42]. Nevertheless, because single-crystal silicon has a diamond structure in which the crystallographic dependence of the surface energy is modest (the smallest surface energy ratio is $\gamma_{\{111\}}/\gamma_{\{100\}} = 1/\sqrt{3}$ [43]), the cleavage tendency is also generally modest. Therefore, the commonly implemented fracture criteria of maximum K_{I} and zero K_{II} were used in this study to predict the crack growth direction. Consequently, the driving force for crack growth was determined from the SIF range ΔK, defined by

$$\Delta K = K_{\sigma,\max} - K_{\sigma,\min} \tag{8}$$

where $K_{\sigma,\max}$ and $K_{\sigma,\min}$ are the maximum and minimum tensile SIFs in a given loading cycle, respectively. It has been argued that the crack growth behavior of brittle materials exhibits a much stronger dependence on $K_{\sigma,\max}$ than ΔK [44]. In addition, as the crack faces come into contact during the compressive portion of a loading cycle, the resulting $K_{\sigma,\min}$ is at least an order of magnitude smaller than $K_{\sigma,\max}$ in the tensile portion of the cycle. Accordingly, the driving force for fatigue crack propagation ΔK was set equal to $K_{\sigma,\max}$, i.e., the maximum tensile SIF arising when the crack was fully open.

3. Results and discussion

Fig. 4 shows a comparison of analytical (Eqs. (5) and (6)) and FEM results of the tensile and shear SIFs, K_σ and K_τ, respectively, versus kink angle φ measured from the initial crack plane. The results are in good agreement, especially for $|\varphi| < 15^\circ$. Since all the calculated kink angles during the simulated crack growth were found to be less than 15° (as shown below), the analytical method based on Eq. (5) was used to determine $K_{\sigma,\max}$ and the corresponding kink angle, which was rounded off to the nearest integer. It is also noted that $K_{\sigma,\max}$ occurred for $\varphi \approx 0^\circ$, at which kink angle $K_\tau \approx 0$.

Because the orientation of the initial crack was randomly varied, it was necessary to examine different textures in the critical beam-anchor region of the beam to determine the highest value of $K_{\sigma,\max}$, hereafter denoted by max $K_{\sigma,\max}$. Considering the periodicity of the effective

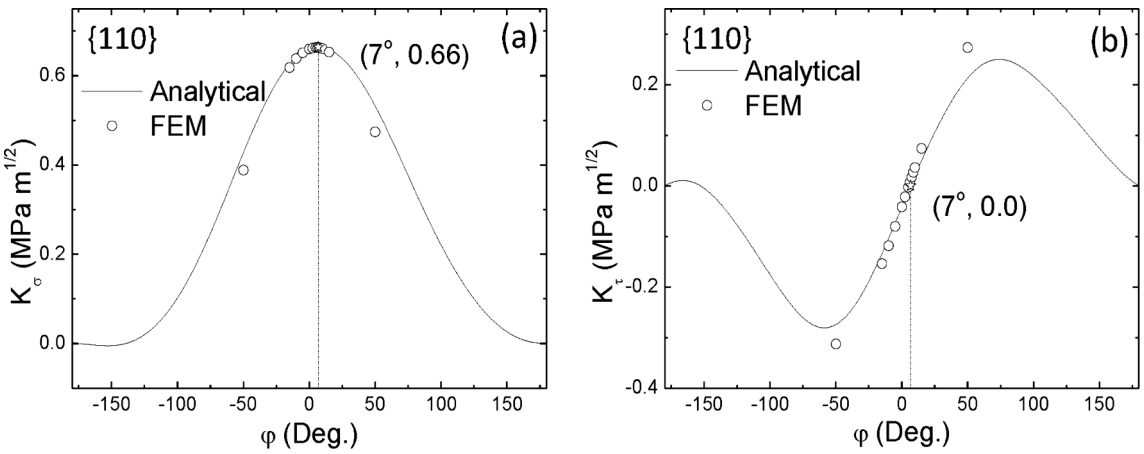

Fig. 4. Analytical and FEM results of (a) the tensile stress intensity factor K_σ and (b) the shear stress intensity factor K_τ versus kink angle φ measured from the initial crack plane for {1 1 0} texture (star symbols correspond to the analytically determined direction of $K_{\sigma,\max}$).

elastic modulus (Fig. 3), the orientation of each grain in the critical region was uniformly varied in the 0–180° and 0–90° range for the {1 1 0} and {1 0 0} texture, respectively. Consequently, 20 FEM models of each texture with randomly generated PVD microstructures in the beam-anchor region were used to compute $K_{\sigma,\max}$. At that juncture, the model that yielded the max $K_{\sigma,\max}$ was modified by varying only the orientation angle of grain (1) from 0 to 180° in 20° increments for the {1 1 0} texture and from 0 to 90° in 10° increments for the {1 0 0} texture. Accordingly, two data sets of $K_{\sigma,\max}$ and associated kink angle φ were generated – a *randomized* set obtained from the randomly generated FEM models and a *fixed* set obtained from the FEM models with grain orientations those of the model that yielded the max $K_{\sigma,\max}$ but with a varying orientation of grain (1).

Fig. 5 shows the kink angle φ and $K_{\sigma,\max}$ as functions of the orientation angle θ of grain (1) for {1 1 0} texture. The data indicate that both φ and $K_{\sigma,\max}$ were mainly determined by the orientation of grain (1), which contained the crack. In all simulation cases of the {1 1 0} texture, $\varphi < 15°$ and the variation of $K_{\sigma,\max}$ resembled that of the effective elastic modulus for the {1 1 0} texture (Fig. 3), implying a strong dependence of $K_{\sigma,\max}$ on the effective elastic modulus of grain (1), i.e., a secondary effect of the orientation of neighboring grains. Fig. 6 shows the variation of φ and $K_{\sigma,\max}$ with the orientation angle θ of grain (1) for {1 0 0} texture. Similar to the {1 1 0} texture, both φ and $K_{\sigma,\max}$ were mainly determined by the orientation of grain (1) and the variation of $K_{\sigma,\max}$ was similar to that of the effective elastic modulus for {1 0 0} texture. However, the variation of $K_{\sigma,\max}$ for {1 0 0} texture was less than that for {1 1 0} texture and $\varphi \approx 9°$ almost throughout the entire range of θ. The foregoing trends can be attributed to less variation in effective modulus for {1 0 0} than {1 1 0} texture (Fig. 3). Considering the exponential dependence of the crack growth rate on $K_{\sigma,\max}$, a strong dependence of the fatigue crack growth rate on the texture of the grain containing the growing crack can be presumed. Moreover, the relatively narrow range of variation of φ for both textures suggested that the crack growth direction was mainly determined by the geometry and boundary conditions at the beam-anchor edge instead of the local grain texture.

Considering the negligibly small effect of the far-field grains on $K_{\sigma,\max}$, the variation of max $K_{\sigma,\max}$ with the orientation angle of the neighboring grains (2)–(6) of grain (1) (Fig. 2(c)) was examined to obtain additional insight into the effect of local texture on crack growth. Because $K_{\sigma,\max}$ exhibited two peaks for {1 1 0} texture (Fig. 5(b)), two cases with similar $K_{\sigma,\max}$ but different kink angles (henceforth referred to as cases (1) and (2) of the {1 1 0} texture) were examined. Table 1 gives the calculated orientation angles of the neighboring grains that yielded the max $K_{\sigma,\max}$ for both {1 1 0} and {1 0 0} texture.

In addition, to examine the effect of loading on $K_{\sigma,\max}$, different displacements were applied to the beam end attached to the rotational ring. Although the effect of the beam-end displacement on the kink angle was insignificant, Fig. 7 shows a linear variation of $K_{\sigma,\max}$ with the beam-end displacement u for both {1 1 0} and {1 0 0} texture, implying a negligible influence of the intrinsic nonlinear deformation behavior of the beam on crack growth. These results suggested a similar crack growth path for different beam displacements, the only difference being

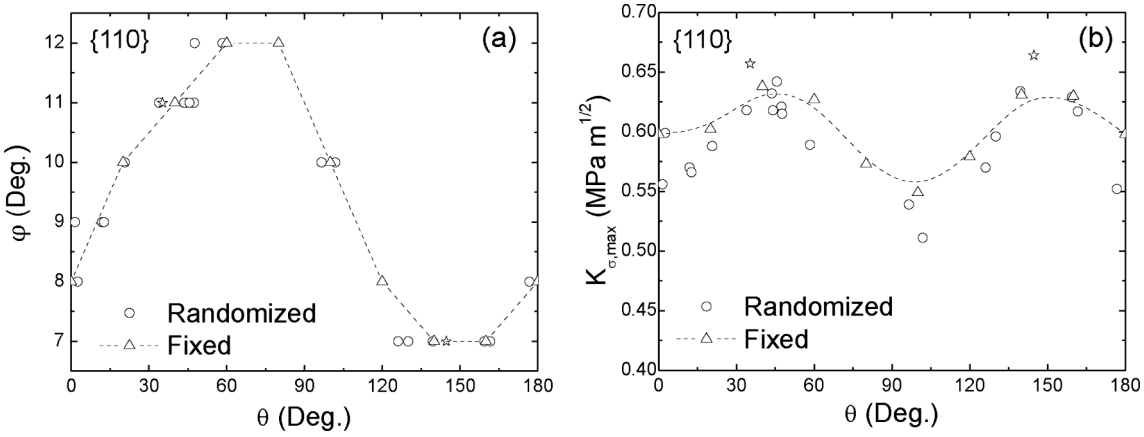

Fig. 5. (a) Kink angle φ and (b) maximum tensile stress intensity factor $K_{\sigma,\max}$ versus orientation angle θ for grain (1) and {1 1 0} texture (star symbols correspond to the direction of $K_{\sigma,\max}$).

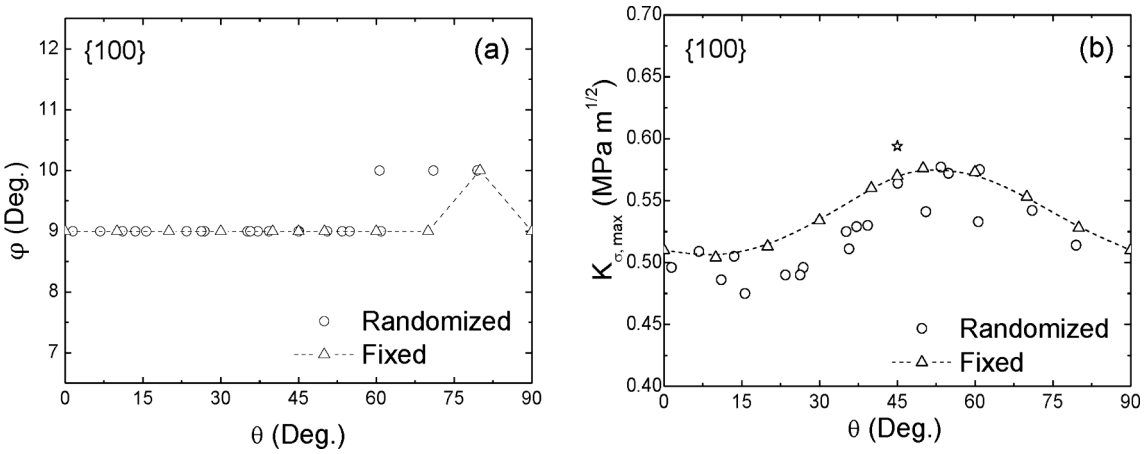

Fig. 6. (a) Kink angle φ and (b) maximum tensile stress intensity factor $K_{\sigma,max}$ versus orientation angle θ for grain (1) and {100} texture (star symbols correspond to local maxima of $K_{\sigma,max}$).

Table 1
Grain orientation angles corresponding to max $K_{\sigma,max}$ for {110} and {100} texture.

Grain	Grain orientation angle, θ (deg.)		
	{110} texture		{100} texture
	case (1)	case (2)	
1	144	36	45.0
2	60	60	67.5
3	90	90	22.5
4	120	120	45.0
5	60	60	67.5
6	144	144	45.0

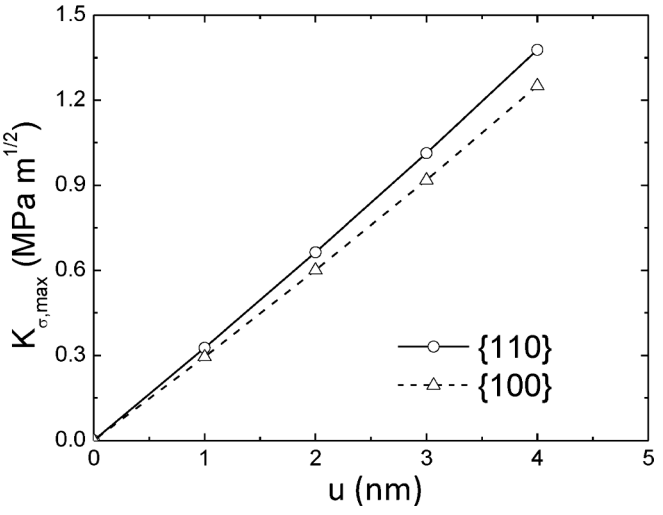

Fig. 7. Maximum tensile stress intensity factor $K_{\sigma,max}$ versus beam tip displacement u for {110} and {100} texture. For all beam tip displacements, both {110} and {100} texture show a constant kink angle equal to 7° and 9°, respectively.

the magnitude of $K_{\sigma,max}$, calculated by the linear interpolation method mentioned previously. For that reason, fatigue crack growth was analyzed for a beam-end displacement equal to 2 μm.

Simulations of the crack advancement encompassed sequential remeshing. After using the analytical method discussed in section 2.5 to determine the kink angle of the existing crack, the FEM mesh was modified by incorporating a crack length increment Δa in the direction of the analytically predicted kink angle. This procedure was repeated in each step of incremental crack growth until the crack propagated to the grain boundary. The selection of an appropriate crack length increment was critical because it could affect the simulated crack path. In the absence of an established approach, two crack length increments that were an order of magnitude smaller than the mean grain diameter (0.38 μm), i.e., $\Delta a = 30$ and 60 nm, were used in the simulations for grain orientation angles θ corresponding to the max $K_{\sigma,max}$ in grain (1) and both {110} and {100} textures (Table 1). Fig. 8 shows crack paths through grain (1) obtained from the foregoing simulations. There are several important findings worthy of mentioning. First, the extremely small spacing (<2 nm) between the crack paths for {110} texture, $\theta = 144°$, and $\Delta a = 30$ and 60 nm, indicated a negligible effect of the crack length increment on crack growth. Consequently, to reduce the computational time, Δa was set equal to 60 nm in all simulations. Second, despite significant differences in the initial kink angle, crack growth followed approximately straight paths, evinced by the very small kink angles (<2°) obtained in each increment step. Third, although the crack paths appeared to differ appreciably from each other, this was only due to the scale used to plot the data. In view of the close similarity of the crack paths, despite the significantly different initial kink angles, it may be inferred that the texture effect on the crack path through grain (1) was minor. Although the polycrystalline microstructure exhibited a

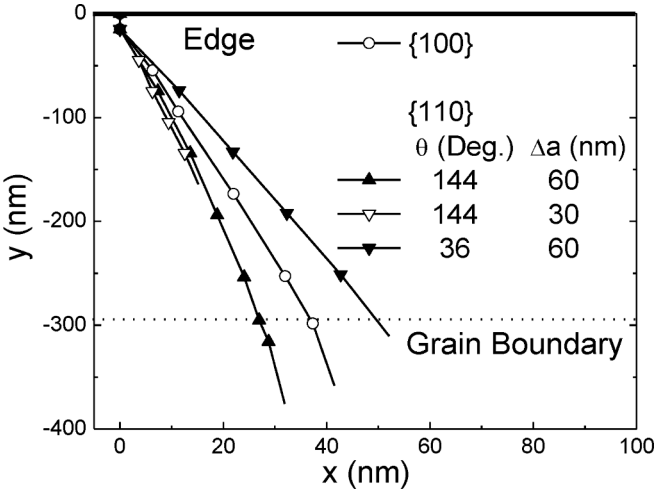

Fig. 8. Crack path in the first two neighboring grains for different in-plane orientation angles θ of grain (1), crack length increment Δa, and {100} and {110} texture.

strong effect on the stress field in the beam-anchor region, the kink angle was more sensitive to the far-field stresses rather than the local stresses.

In addition to the similar crack paths, Fig. 9 shows almost identical variation of $K_{\sigma,\max}$ with crack length a for all simulation cases with {1 1 0} texture and small differences with the simulation case with {1 0 0} texture, further validating the selection of $\Delta a =$ 60 nm in all simulations. Notably, all simulation cases demonstrated a square root dependence of $K_{\sigma,\max}$ on crack length. Since the kink angle from the initial crack was small (i.e., in the range of 7–9°) for both textures (Figs. 5(a) and 6(a)), the direction of maximum K_{I} was essentially unaffected by the distribution of the grain orientation angle; thus, the crack advanced almost in a straight line within grain (1) after diverging from the initial crack that was perpendicular to the beam edge. Consequently, it was the far-field stress distribution (controlled by the beam geometry and the boundary conditions) that determined the crack growth direction rather than the local texture. Fig. 9 also shows that the {1 1 0} texture yielded higher $K_{\sigma,\max}$ values than the {1 0 0} texture for a given crack length, evidently due to the higher effective stiffness of the {1 1 0} texture (Fig. 3), implying faster crack growth for {1 1 0} texture. Moreover, despite the differences in initial kink angles and crack growth paths corresponding to cases (1) and (2) of the {1 1 0} texture (Table 1), these simulation cases demonstrated essentially identical variations in $K_{\sigma,\max}$ with crack length.

Since cases (1) and (2) yielded almost identical crack growth through grain (1), case (1) of the simulations with {1 1 0} texture was selected to further study the grain boundary effect on crack growth. When the crack impinged onto the grain boundary, the crack growth direction was controlled by the effective SIF K_{eff}, because K_σ and K_τ were of the same order of magnitude. For a given kink angle φ, K_{eff} is defined by

$$K_{\mathrm{eff}}(\varphi) = \sqrt{K_\sigma^2 + K_\tau^2} \tag{9}$$

Fig. 10 shows analytical and FEM results of K_{eff} versus φ for grain (4), which is neighbor to grain (1) (Fig. 2), for {1 1 0} and {1 0 0} texture. In addition to the good agreement between the results of the two approaches, the maximum value of K_{eff} (designated by $K_{\mathrm{eff}}^{\max}$) corresponded to $\varphi \approx 1°$ and –2° for {1 1 0} and {1 0 0} texture, respectively, implying that $K_{\mathrm{eff}}^{\max}$ essentially ascended in the main crack direction. In addition, K_{eff} along the grain boundary (denoted by K_{eff}^{gb}) was approximately 19% and 29% smaller than the corresponding $K_{\mathrm{eff}}^{\max}$ for {1 1 0} and {1 0 0} texture, respectively. To determine the range of $K_{\mathrm{eff}}^{gb}/K_{\mathrm{eff}}^{\max}$, at least 20 randomized FEM simulations were performed for each texture. Fig. 11 displays the variation of $K_{\mathrm{eff}}^{\max}$ with the orientation angle of grain (4) for {1 1 0} and {1 0 0} texture obtained from the foregoing simulations. Based on the results shown in Fig. 11, the mean value of $K_{\mathrm{eff}}^{gb}/K_{\mathrm{eff}}^{\max}$ was found equal to 1.29 and 1.37 for {1 1 0} and {1 0 0} texture, respectively. When the crack tip impinged onto the boundary of grains (1) and (4), more grains were within the K-dominant zone of the crack tip, affecting the fracture process to some degree. Consequently, there was no strong correlation between kink angle, SIF, and orientation angle of grain (4).

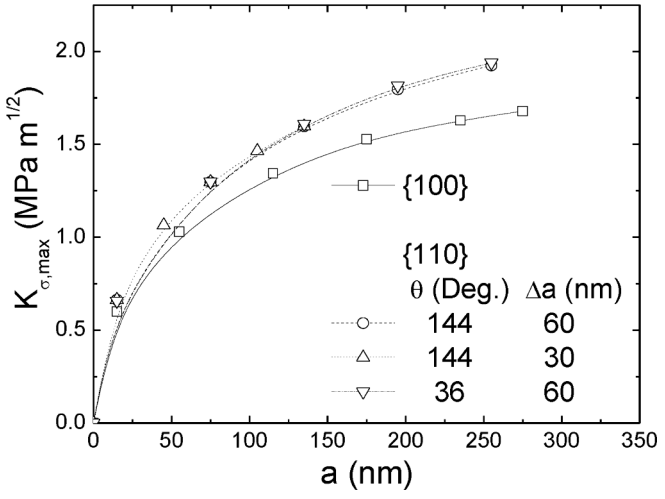

Fig. 9. Maximum tensile stress intensity factor $K_{\sigma,\max}$ versus crack length a for {1 0 0} and {1 1 0} texture and different in-plane orientation angles θ of grain (1) and crack length increments Δa.

For a polycrystalline material, crack growth along a grain boundary occurs when the following condition is satisfied

$$\frac{K_{\mathrm{eff}}^{gb}}{K_{\mathrm{eff}}^{\max}} \geq \sqrt{\frac{E_{gb}^{\mathrm{eff}} G_{gb}}{E_c^{\mathrm{eff}} G_g}} \tag{10}$$

where E_{gb}^{eff} and E_c^{eff} are the effective elastic modulus in the direction normal to the grain boundary and the crack, respectively, and G_{gb} and G_g denote the critical energy release rate of the grain boundary and grain, respectively. Generally, $G_{gb} < G_g$ and the ratio G_{gb}/G_g strongly depends on the fabrication process. Since $K_{\mathrm{eff}}^{\max}$ was only 30–40% higher than K_{eff}^{gb}, either transgranular or intergranular crack growth could be predicted. However, in the absence of experimental measurements of the fracture resistance of the polysilicon grain boundary, it was presumed that $G_{gb} \approx G_g$. This led to the supposition that crack growth into the next grain, i.e., grain (4), would occur in a direction determined by the magnitude of $K_{\mathrm{eff}}^{\max}$. Indeed, as shown in Fig. 8 for $\theta = 144°$ and {1 1 0} texture, the crack propagated into grain (4) following approximately the same straight path as in grain (1).

Fig. 12 shows $K_\sigma^{\max}$ as a function of crack length a for crack growth from grain (1) into grain (4) and {1 1 0} texture. It is noted that the monotonic increase of $K_\sigma^{\max}$ with a during crack growth inside grain (1) was interrupted when the crack tip reached the vicinity of the grain boundary. The decrease in $K_\sigma^{\max}$ at the instant the crack impinged onto the grain boundary was due to the decrease of E_1^{eff} as the crack propagated into a different grain. This finding suggested a non-monotonic increase in crack growth rate through the silicon grains (transgranular fracture). However, if $G_{gb} < G_g$, the crack would markedly deviate from the original path and will grow along the grain boundary (intergranular fracture) despite the existence of the maximum SIF in the grain. An interface cohesive zone model of the grain boundaries can be incorporated in future PVD-FEM analyses to investigate the competition between transgranular and intergranular fracture for different textures.

The present PVD-FEM analysis of crack growth under multi-axial loading is based on the validity of LEFM, which presumes linear elastic material behavior, except in a vanishingly small region ahead of the crack tip, known as the process zone or plastic zone, where the material exhibits significant inelastic behavior. However, when the process zone is small relative to the crack length, LEFM still holds and the stress state can be described by the SIF. Thus, the current analysis can also be applied to materials demonstrating limited crack-tip plasticity. Alternatively, when the process zone at the crack tip is large, an elastic–plastic fracture mechanics approach based on other parameters, such as the crack-tip opening displacement and the J-integral, must be incorporated in the PVD-FEM analysis, under the condition that the stress increases monotonically throughout the fracturing component up to the instant of crack extension (i.e., no unloading).

4. Conclusions

A PVD-FEM analysis of crack growth in polysilicon micromachines was performed to elucidate the microstructure effect on fatigue cracking under multi-axial loading. Based on the presented analytical and simulation results and pertinent discussions, the following main conclusions can be drawn from this study.

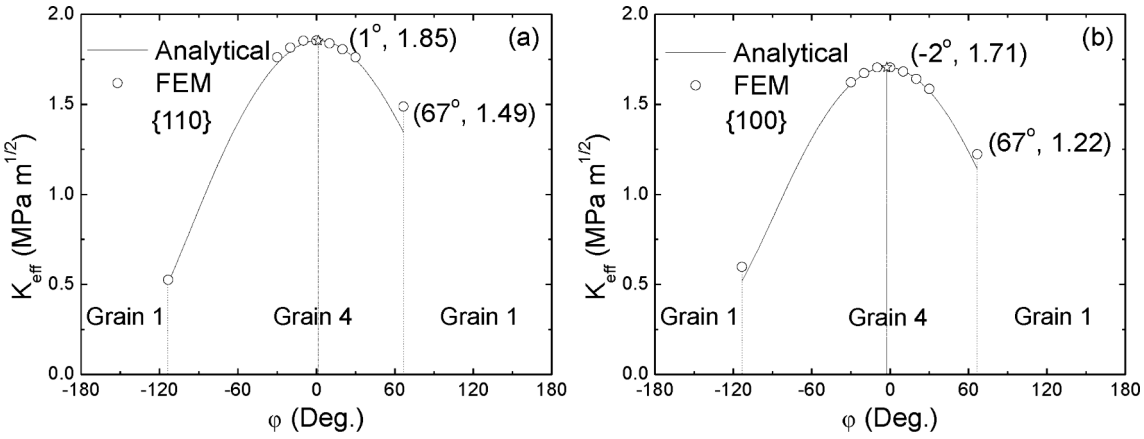

Fig. 10. Analytical and FEM results of the effective stress intensity factor K_{eff} versus kink angle φ at the instant of crack impingement onto the common boundary of grains (1) and (4) for (a) {1 1 0} and (b) {1 0 0} texture.

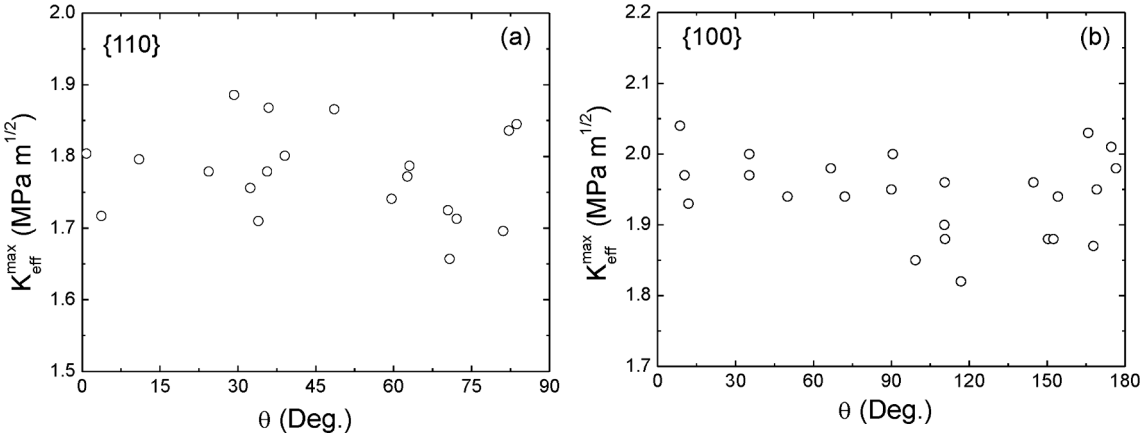

Fig. 11. Maximum effective stress intensity factor $K_{\text{eff}}^{\max}$ versus orientation angle θ of grain (4) for (a) {1 1 0} and (b) {1 0 0} texture.

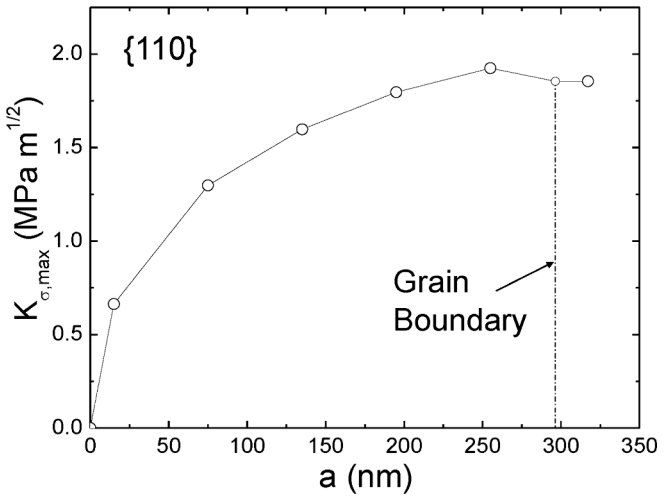

Fig. 12. Maximum tensile stress intensity factor $K_{\sigma,\max}$ versus crack length a during crack growth from grain (1) into grain (4) for {1 1 0} texture.

1. During subcritical crack initiation, the effective elastic modulus of a grain containing a submicrometer crack exhibited a strong effect on the magnitude of the SIF (i.e., crack growth rate), whereas the effect of neighboring grains was secondary. A larger variation in kink angle was observed for {1 1 0} texture than {1 1 0} texture due to more pronounced variation of the effective elastic modulus with grain orientation angle.
2. While the crack path within a grain was almost straight and nearly insensitive to the local texture, the driving force for crack advancement $K_{\sigma,\max}$ was affected by the texture, with the {1 1 0} texture showing higher $K_{\sigma,\max}$ values than the {1 0 0} texture. However, both textures demonstrated a similar dependence of $K_{\sigma,\max}$ on the crack length.
3. When the crack tip reached the grain boundary, the effective SIF K_{eff} was affected not only by the grain just ahead of the crack but also by all neighboring grains. Depending on the angle between the propagating crack and the grain boundary, the critical energy release rate of the grain and the grain boundary and the corresponding elastic modulus, both transgranular and intergranular fracture could be encountered in polycrystalline silicon.
4. For the simulated transgranular fracture, an abrupt decrease in $K_{\sigma,\max}$ occurred when the crack penetrated a neighboring grain, implying non-monotonic crack growth through the polysilicon microstructure.
5. The computational methodology developed in this study can be used to perform fracture mechanics analyses of microstructures subjected to multi-axial loading with the local texture incorporated in the critical region(s) of the microstructures.

Declaration of Competing Interest

The authors declare that they have no known competing financial interests or personal relationships that could have appeared to influence

the work reported in this paper.

Data availability

Data will be made available on request.

Acknowledgements

This work was funded by the National Science Foundation (NSF) under Grant No. DMI-9872324 and the Defense Advanced Research Projects Agency (DARPA) under Grant No. DABT63-98-1-0011.

References

[1] Wilson CJ, Ormeggi A, Narbutovskih M. Fracture testing of silicon microcantilever beams. J Appl Phys 1996;79:2386–93.
[2] Wilson CJ, Beck PA. Fracture testing of bulk silicon microcantilever beams subjected to a side load. J Microelectromech Syst 1996;5:142–50.
[3] Connally JA, Brown SB. Slow crack growth in single-crystal silicon. Science 1992; 256:1537–8.
[4] Muhlstein CL, Brown SB, Ritchie RO. High-cycle fatigue of single-crystal silicon thin films. J Microelectromech Syst 2001;10:593–600.
[5] Muhlstein CL, Stach EA, Ritchie RO. Mechanism of fatigue in micron-scale films of polycrystalline silicon for microelectromechanical systems. Appl Phys Lett 2002; 80:1532–4.
[6] Brown SB, Van Arsdell W, Muhlstein CL. Materials reliability in MEMS devices. Proc Int Conf Solid-State Sens Actuat, Transducers 1997:591–3.
[7] Van Arsdell WW, Brown SB. Subcritical crack growth in silicon MEMS. J Microelectromech Syst 1999;8:319–27.
[8] White CD, Xu R, Sun X, Komvopoulos K. Dynamic MEMS devices for multi-axial fatigue and elastic modulus measurement. Proc SPIE 2003;4980:63–74.
[9] White CD, Xu R, Sun X, Komvopoulos K. Characterization of microscale material behavior with MEMS resonators. Proc Nanotechnol Conf 2003;1:494–7.
[10] McKinstry HA, Shull HE, Buessem WR. Localized stress in elastic polycrystalline materials. Nucl Metall 1976;20:695–705.
[11] McKinstry HA, Shull HE, Buessem WR. Stress and strain fields in idealized polycrystalline materials and the prediction of fracture initiation sites. Nucl Metall 1976;20:929–41.
[12] Tvergaard V, Hutchinson JW. Microcracking in ceramics induced by thermal expansion or elastic anisotropy. J Amer Ceram Soc 1988;71:157–66.
[13] Li X-D. *K* variations and anisotropy: Microstructure effect and numerical predictions. ASME J Eng Mater Technol 2003;125:65–74.
[14] Yamamoto M, Kitamura T, Ogata T. Influence of microscopically distributed inhomogeneity and anisotropy of grains on high-temperature crack propagation properties of directionally solidified superalloy. Eng Fract Mech 2008;75:779–89.
[15] Mullen RL, Ballarini R, Yin Y, Heuer AH. Monte Carlo simulation of effective elastic constants of polycrystalline thin films. Acta Mater 1997;45:2247–55.
[16] Ballarini R, Mullen RL, Heuer AH. The effects of heterogeneity and anisotropy on the size effect in cracked polycrystalline films. Int J Fract 1999;95:19–39.
[17] Kumar S, Kurtz SK, Agarwala VK. Micro-stress distribution within polycrystalline aggregate. Acta Mech 1996;114:203–16.
[18] Xu R, Komvopoulos K. A Poisson–Voronoi-based finite element stress analysis of resonating polysilicon micromachines. Acta Mech 2023 (accepted).
[19] Belytschko T, Organ D, Gerlach C. Element-free Galerkin methods for dynamic fracture in concrete. Comp Meth Appl Mech Eng 2000;187:385–99.
[20] Sukumar N, Prévost J-H. Modeling quasi-static crack growth with the extended finite element method. Part I: Computer implementation. Int J Solids Struct 2003; 40:7513–37.
[21] Moës N, Dolbow J, Belytschko T. A finite element method for crack growth without remeshing. Int J Numer Meth Eng 1999;46:131–50.
[22] Xu X-P, Needleman A. Numerical simulations of fast crack growth in brittle solids. J Mech Phys Solids 1994;42:1397–434.
[23] Camacho GT, Ortiz M. Computational modelling of impact damage in brittle materials. Int J Solids Struct 1996;33:2899–938.
[24] Espinosa HD, Zavattieri PD. A grain level model for the study of failure initiation and evolution in polycrystalline brittle materials. Part I: Theory and numerical implementation. Mech Mater 2003;35:333–64.
[25] Espinosa HD, Zavattieri PD. A grain level model for the study of failure initiation and evolution in polycrystalline brittle materials. Part II: Numerical examples. Mech Mater 2003;35:365–94.
[26] Gallo P, Hagiwara Y, Shimada T, Kitamura T. Strain energy density approach for brittle fracture from nano to macroscale and breakdown of continuum theory. Theor Appl Fract Mech 2019;103:102300.
[27] Kamins TI. Structure and properties of LPCVD silicon films. J Electrochem Soc 1980;127:686–90.
[28] Krulevitch P, Nguyen TD, Johnson GC, Howe RT, Wenk HR, Gronsky R. LPCVD polycrystalline silicon thin films: The evolution of structure, texture and stress. Proc Mater Res Soc 1990;202:167–72.
[29] Nagasima N, Kubota N. Structures of Si films chemically vapor-deposited on amorphous SiO_2 substrates. Jap J Appl Phys 1975;14:1105–12.
[30] Hibbitt, Karlsson, Sorensen. ABAQUS/Standard User's Manual. 5.8 ed. Pawtucket, RI, 1998.
[31] Jayaraman S, Edwards RL, Hemker KJ. Relating mechanical testing and microstructural features of polysilicon thin films. J Mater Res 1999;14:688–97.
[32] Maier-Schneider D, Köprülülü A, Holm S, Obermeier E. Elastic properties and microstructure of LPCVD polysilicon films. J Micromech Microeng 1996;6:436–46.
[33] Kahn H, He AQ, Heuer AH. Homogeneous nucleation during crystallization of amorphous silicon produced by low-pressure chemical vapour deposition. Philo Mag A 2002;82:137–65.
[34] Pampuch R. Constitution and properties of ceramic materials. New York, NY: Elsevier; 1991.
[35] Ting T.C.T. Invariants of anisotropic elastic constants. Quart J Mech Appl Math 1987;40:431–48.
[36] Ting TCT. Anisotropic elastic constants that are structurally invariant. Quart J Mech Appl Math 2000;53:511–23.
[37] Hirsekorn S. Elastic properties of polycrystals. A review Text Microstruct 1990;12: 1–14.
[38] Chan SK, Tuba IS, Wilson WK. On the finite element method in linear fracture mechanics. Eng Fract Mech 1970;2:1–17.
[39] Azhdari A, Nemat-Nasser S. Hoop stress intensity factor and crack-kinking in anisotropic brittle solids. Int J Solids Struct 1996;33:2023–37.
[40] Obata M, Nemat-Nasser S, Goto Y. Branched cracks in anisotropic elastic solids. ASME J Appl Mech 1989;56:858–64.
[41] Azhdari A, Nemat-Nasser S. Experimental and computational study of fracturing in an anisotropic brittle solid. Mech Mater 1998;28:247–62.
[42] Azhdari A, Nemat-Nasser S, Rome J. Experimental observations and computational modeling of fracturing in an anisotropic brittle crystal (sapphire). Int J Fract 1998; 94:251–66.
[43] Lawn B. Fracture of brittle solids. 2nd ed. Cambridge, UK: Cambridge University Press; 1993.
[44] Ritchie RO, Gilbert CJ, McNaney JM. Mechanics and mechanisms of fatigue damage and crack growth in advanced materials. Int J Solids Struct 2000;37: 311–29.